Linear stability, transient energy growth, and the role of viscosity stratification in compressible plane Couette flow

M. Malik and J. Dey
Department of Aerospace Engineering, Indian Institute of Science, Bangalore 560012, India

Meheboob Alam*
Engineering Mechanics Unit, Jawaharlal Nehru Center for Advanced Scientific Research, Jakkur P.O., Bangalore 560064, India

(Received 14 August 2007; revised manuscript received 9 January 2008; published 31 March 2008)

Linear stability and the nonmodal transient energy growth in compressible plane Couette flow are investigated for two prototype mean flows: (a) the *uniform shear* flow with constant viscosity, and (b) the *nonuniform shear* flow with *stratified* viscosity. Both mean flows are linearly unstable for a range of supersonic Mach numbers (M). For a given M, the critical Reynolds number (Re) is significantly smaller for the uniform shear flow than its nonuniform shear counterpart; for a given Re, the *dominant* instability (over all streamwise wave numbers, α) of each mean flow belongs to different modes for a range of supersonic M. An analysis of perturbation energy reveals that the instability is primarily caused by an excess transfer of energy from mean flow to perturbations. It is shown that the energy transfer from mean flow occurs close to the moving top wall for "mode I" instability, whereas it occurs in the bulk of the flow domain for "mode II." For the nonmodal transient growth analysis, it is shown that the maximum temporal amplification of perturbation energy, $G_{\max}$, and the corresponding time scale are significantly larger for the uniform shear case compared to those for its nonuniform counterpart. For $\alpha=0$, the linear stability operator can be partitioned into $\mathcal{L}\sim\bar{\mathcal{L}}+\mathrm{Re}^2\,\mathcal{L}_p$, and the Re-dependent operator $\mathcal{L}_p$ is shown to have a negligibly small contribution to perturbation energy which is responsible for the validity of the well-known quadratic-scaling law in uniform shear flow: $G(t/\mathrm{Re})\sim\mathrm{Re}^2$. In contrast, the dominance of $\mathcal{L}_p$ is responsible for the invalidity of this scaling law in nonuniform shear flow. An inviscid reduced model, based on Ellingsen-Palm-type solution, has been shown to capture all salient features of transient energy growth of full viscous problem. For both modal and nonmodal instability, it is shown that the *viscosity stratification* of the underlying mean flow would lead to a delayed transition in compressible Couette flow.

DOI: 10.1103/PhysRevE.77.036322 PACS number(s): 47.15.Fe, 47.20.Ft, 47.40.Ki

I. INTRODUCTION

The transition to turbulence has its genesis to the growth of small disturbances in an otherwise undisturbed laminar flow. Hence, an understanding of different mechanisms of instability growth is important to determine the transition scenarios that eventually lead to turbulence in fluids. The linear stability theory, via the standard normal-mode approach, is the starting point of such analyses which predict the onset of the growth of a small perturbation imposed on a laminar flow [1]. However, there are flow configurations that are stable according to the linear stability theory (i.e., the critical Reynolds number is infinity, $\mathrm{Re}_{\mathrm{cr}}=\infty$) for which the experiments show a finite $\mathrm{Re}_{\mathrm{cr}}$ ($\ll\infty$). It is reasonable to assume that such subcritical flows may be destabilized by the nonlinear effects that are neglected in the linear theory. Is there any linear mechanism that causes an infinitesimally small perturbation already present in the flow to grow substantially for a short time? If this is true, then the nonlinearities could take over subsequently to trigger a flow transition.

Indeed, following the seminal work of Orr [2], it has recently been realized that one should investigate the short-time dynamics of the flow without *a priori* assuming the exponential time dependence for perturbations. The key idea is that even though each eigenmode decays in the asymptotic limit ($t\to\infty$) for a *stable* flow, a superposition of such stable eigenmodes has potential for large *transient* energy growth before they can be stabilized by the viscosity. Such transient growth analyses [3–12] have revealed that a flow can sustain large amplification of perturbation energy even if the flow is linearly stable. In mathematical terms, the underlying linear stability operator is nonnormal (non-self-adjoint) [4,5,13], which is responsible for transient energy growth. This is a possible route to flow transition for subcritical flows which has become an active field of research during the last ten years [13–15].

It is known that small changes in the mean flow can be stabilizing or destabilizing, which is an attractive avenue from the viewpoint of controlling or manipulating instabilities. A recent work [16] clearly underscores the effects of mean-flow variation on the stability of *incompressible* plane Couette flow—using the concept of pseudospectra [5,6], these authors showed that relatively small changes in the mean flow could be *destabilizing*. Another important issue in stability research is the possible role of viscosity stratification on instabilities which has a stabilizing effect, leading to a delayed transition. In incompressible non-Newtonian fluids, the role of viscosity stratification in delaying transition is currently debated for which we refer to a recent work [17].

The above issues have not been investigated for *compressible* fluids in a systematic manner. In this paper, the

*Corresponding author. meheboob@jncasr.ac.in

 ©2008 The American Physical Society

linear stability characteristics and the nonmodal transient energy growth in the compressible plane Couette flow are analyzed for two prototype model problems: (a) uniform shear flow with constant viscosity and (b) nonuniform shear flow with stratified viscosity. The *first* goal of the present work is to understand the similarities and differences of the modal and nonmodal stability characteristics between these two closely related mean flows of a compressible fluid. The *second* goal is to reveal the role of *viscosity stratification* on instabilities in a *compressible* fluid since we have two prototype mean-flow configurations in which one has a *stratified* viscosity across the channel and the other has a constant viscosity. The *third* goal is to characterize the underlying instability mechanism in compressible Couette flow via an energy analysis.

This paper is organized as follows. The governing equations and the mean flow are briefly described in Sec. II. The linear stability problem is formulated in Sec. III, and the related results are presented in Sec. III. The results on the transient energy growth are presented in Sec. IV. The summary and conclusions are provided in Sec. V.

II. EQUATIONS OF MOTION AND MEAN FLOW

Consider a perfect gas of density ρ^* and temperature T^* between two walls that are separated by a distance h^*: the top wall moves with a velocity U_1^* and the lower wall is stationary, with the top-wall temperature being maintained at T_1^*; here the superscript $*$ denotes dimensional quantities, and the subscript 1 refer to the quantities at the top wall. Let u^*, v^*, and w^* be the velocity components in the streamwise (x^*), wall-normal (y^*), and spanwise (z^*) directions, respectively. The conservation equations for the mass, momentum, and energy, in dimensionless form, are

$$\frac{\partial \rho}{\partial t} = -\nabla \cdot (\rho \mathbf{u}), \tag{1}$$

$$\rho \frac{Du_i}{Dt} = -\frac{1}{\gamma M^2}\frac{\partial p}{\partial x_i} + \frac{1}{\mathrm{Re}}\left[\mu \nabla^2 u_i + \frac{\partial}{\partial x_i}(\lambda \nabla \cdot \mathbf{u}) + \mu \frac{\partial}{\partial x_i}(\nabla \cdot \mathbf{u}) + (\nabla \mu) \cdot (\nabla u_i) + (\nabla \mu) \cdot \frac{\partial \mathbf{u}}{\partial x_i}\right], \tag{2}$$

$$\rho \frac{DT}{Dt} = (1-\gamma) p \nabla \cdot \mathbf{u} + \frac{\gamma}{\mathrm{Re}} \nabla \cdot \left(\frac{\mu}{\sigma} \nabla T\right) + \Phi, \tag{3}$$

with $D/Dt = (\partial/\partial t + \mathbf{u} \cdot \nabla)$ being the material derivative, Φ the dissipative shear work, and the equation of state is that of a perfect gas: $p = \rho T$. We have used the separation between the two walls h^* as the length scale, the top wall velocity, U_1^*, and temperature, T_1^*, as the velocity and temperature scale, respectively, and the inverse of the overall shear rate, U_1^*/h^*, as the time scale. The nondimensional control parameters are the Reynolds number Re, the Prandtl number σ, and the Mach number M,

$$\mathrm{Re} = \frac{\rho_1^* U_1^* h^*}{\mu_1^*}, \quad \sigma = \frac{\mu^* c_p^*}{\kappa^*}, \quad \text{and} \quad M = \frac{U_1^*}{\sqrt{\gamma R T_1^*}}. \tag{4}$$

Here μ^* is the shear viscosity, ζ the bulk viscosity, κ^* the thermal conductivity, $\gamma = c_p^*/c_v^*$ the ratio of specific heats, R the universal gas constant, and $\lambda = \zeta - 2\mu/3$. The bulk viscosity is assumed to be zero (i.e., $\zeta = 0$) such that $\lambda = -2\mu/3$ (Stokes' assumption). For all calculations below, $\sigma = 0.72$ and $\gamma = 1.4$.

A. Constant viscosity: Uniform shear flow

For the unidirectional steady and fully developed mean flow, the continuity and the z momentum equations are trivially satisfied. From the y-momentum equation, it is straightforward to verify that the pressure, $p_0 = \rho_0(y) T_0(y)$, is a constant, which is normalized such that $p_0 = 1$. (The subscript 0 is used to designate the mean flow quantities.) The boundary conditions on the streamwise velocity $U_0(y)$ and temperature $T_0(y)$ are

$$U_0(0) = 0, \quad U_0(1) = 1, \quad T_0(0) = T_w, \quad T_0(1) = 1, \tag{5}$$

with T_w being the temperature of the lower wall.

For the constant viscosity model ($\mu_0 = \text{const}$), the streamwise velocity varies linearly with y,

$$U_0(y) = y, \tag{6}$$

i.e., the shear rate is *uniform*. It is straightforward to verify that the temperature varies quadratically with y,

$$T_0(y) = T_r\left[r + (1-r)y - \left(1 - \frac{1}{T_r}\right)y^2\right], \tag{7}$$

where T_r is the recovery temperature,

$$T_r = 1 + \frac{(\gamma - 1)\sigma M^2}{2}, \tag{8}$$

and $r = T_w/T_r$ the temperature ratio. Note that $r = 1$ corresponds to an adiabatic lower wall.

B. Viscosity stratification: Nonuniform shear flow

For a temperature-dependent viscosity model, for example, with Sutherland's law,

$$\mu(T) = \frac{T^{3/2}(1+C)}{(T+C)}, \quad \text{with } C = 0.5, \tag{9}$$

the streamwise velocity has a nonuniform shear rate. For this case, the mean flow equations,

$$\frac{d}{dy}\left(\mu(T_0)\frac{dU_0}{dy}\right) = 0,$$

$$\sigma^{-1}\frac{d}{dy}\left(\mu\frac{dT_0}{dy}\right) + (\gamma - 1)M^2 \mu \left(\frac{dU_0}{dy}\right)^2 = 0, \tag{10}$$

with boundary conditions (5) have been solved numerically using the fourth-order Runge-Kutta method.

In contrast to the constant viscosity model, for this model the viscosity varies across the channel width, i.e., the mean flow is characterized by a *stratified* viscosity. It is straightforward to verify that the viscosity at the lower wall increases with increasing Mach number, and hence the degree of viscosity stratification increases with increasing M.

III. LINEAR STABILITY ANALYSIS

For the linear stability analysis, the mean flow, $\mathbf{q_0}=(U_0,0,0,\rho_0,T_0)^T$, is perturbed with small-amplitude perturbations $\mathbf{q}=\mathbf{q_0}+\hat{\mathbf{q}}$, and the governing equations (1) to (3) are linearized around the mean flow. Seeking normal mode solutions of the resulting linearized partial differential equations,

$$\hat{\mathbf{q}}(x,y,z,t)=\mathbf{q}'(y)\exp[i(\alpha x+\beta z-\omega t)], \tag{11}$$

we obtain a differential eigenvalue system,

$$\mathcal{L}\mathbf{q}'=\omega I\mathbf{q}', \tag{12}$$

where $\mathcal{L}$ is the linear stability operator, $\mathbf{q}'=\{u',v',w',\rho',T'\}^T$ is the eigenfunction, and I the identity matrix. Here α and β are the streamwise and spanwise wave numbers, respectively, and $\omega=\omega_r+i\omega_i$ is the complex frequency; the phase speed of perturbation is given by $c_r=\omega_r/\alpha$ and the growth or decay rate by ω_i.

The boundary conditions on perturbation variables are taken to be

$$u'(0)=0=u'(1),\quad v'(0)=0=v'(1),$$

$$w'(0)=0=w'(1),\quad T'(1)=0=\frac{dT'}{dy}(0). \tag{13}$$

The Chebyshev spectral method [18] is used to discretize the differential eigenvalue problem, Eqs. (12) and (13) at $(N+1)$ Gauss-Lobotto collocation points, where N is the degree of the Chebyshev polynomial. This yields an algebraic eigenvalue system, $AX=\omega BX$, which is then solved using the QR algorithm of the MATLAB software.

A. Spectra and acoustic modes

Figure 1(a) shows the distribution of eigenvalues, $c=\omega/\alpha=c_r+ic_i$, in the complex plane, and the zoom of Fig. 1(a), portraying the well-known "Y" branch of the viscous modes, is shown in Fig. 1(b). The parameter values are set to $\mathrm{Re}=10^5$, $M=5$, $\alpha=0.1$, and $\beta=0$, with $N=150$. The classification of inviscid eigenvalues (i.e., *acoustic* modes) into *odd* and *even* families in Fig. 1(a) is based on their phase speeds [19]: the *odd modes* (I,III,…) have phase speeds greater than unity in the limit of $\alpha\to 0$, and the *even modes* (II,IV,…) have phase speeds less than zero as $\alpha\to 0$. (Recall that the nondimensional velocity of the top and bottom walls are 1 and 0, respectively.) With increasing α, however, the phase speeds of even and odd modes increase and decrease, respectively (not shown), and these modes become unstable once they enter the viscous range of the spectra (i.e., for $0<c_r<1$) for a range of supersonic Mach numbers and above some critical value of Reynolds number (see below). More specifically, the phase speed of mode I decreases below unity and that of mode II increases above zero, when they degenerate into unstable modes with increasing α. This overall scenario of modal structure holds for both mean flows; however, there are important differences with regard to the unstable zones in different control parameter space, the dominant instability, and the critical Reynolds number as detailed below.

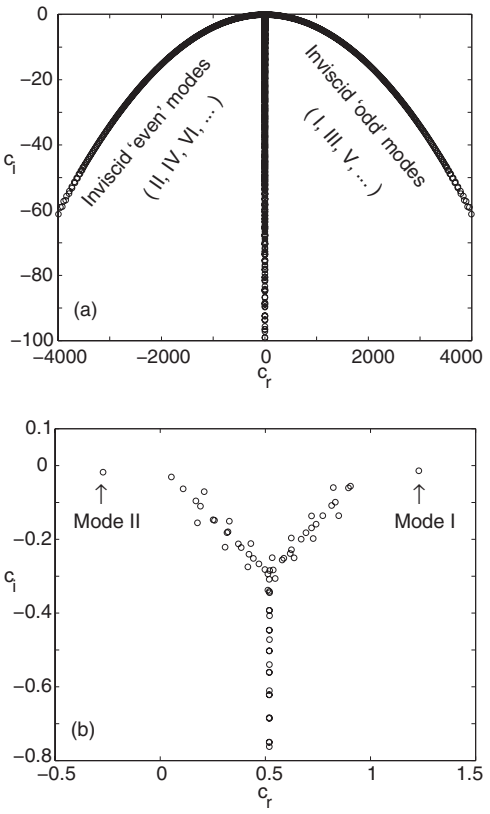

FIG. 1. Distribution of eigenvalues $(c\equiv\omega/\alpha=c_r+ic_i)$ in the complex plane for uniform shear flow with $\mathrm{Re}=10^5$, $M=2$, $\alpha=0.1$, and $\beta=0$. Panel (b) is the zoom of the viscous modes in panel (a). According to the phase-speed-based classification of inviscid modes, mode III stays on the right of mode I, mode IV is on the left of mode II, and so on (see text for details).

B. Stability diagram and dominant instability

Figures 2(a)–2(c) show the contours of the growth rate of the least decaying mode, $\omega_{ldi}=\max(\omega_i)$, in the (M,α) plane for the uniform shear flow with two-dimensional disturbances $(\beta=0)$ at three different Reynolds numbers. The flow is unstable inside the neutral stability contour $(\omega_{ldi}=0)$ and stable outside. With increasing Re, the size of the instability region increases and there is an *additional instability loop* in Fig. 2(c) for $\mathrm{Re}=5\times10^5$. For a comparison, the analog of Fig. 2(c) is displayed in Fig. 2(d) for the nonuniform shear flow. It is seen that the ranges of M and α, over which the flow is unstable, are much larger for the uniform shear flow. Moreover, the *additional unstable loop* at large α in Fig. 2(c) is missing in the stability diagram of the nonuniform shear

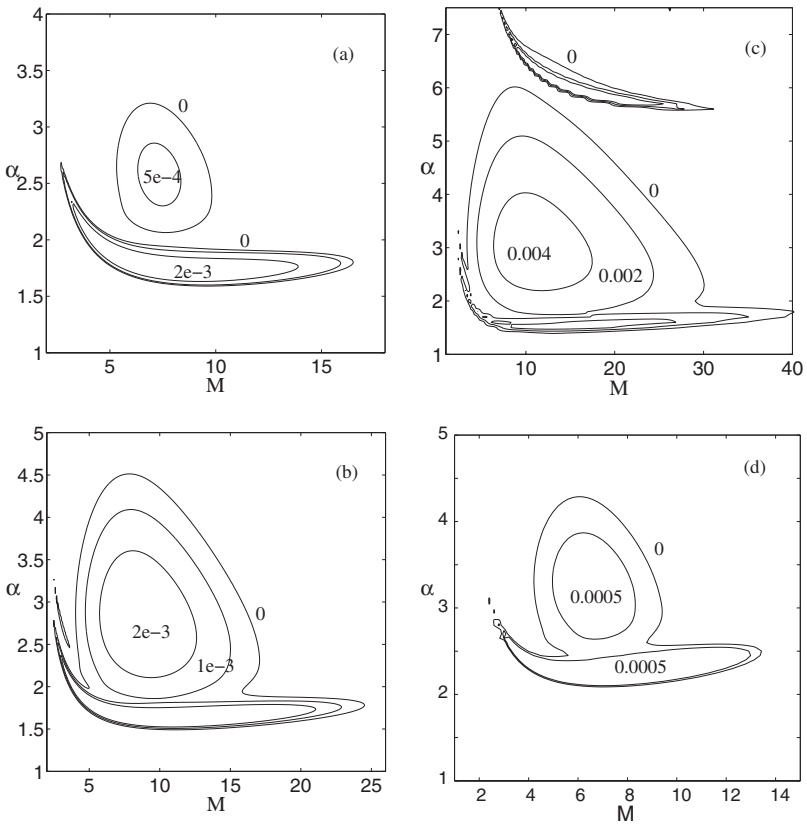

FIG. 2. (a)–(c) Stability maps for the uniform shear flow in the (M,α) plane for two-dimensional $(\beta=0)$ perturbations at different Reynolds numbers: (a) $\mathrm{Re}=10^5$; (b) $\mathrm{Re}=2\times10^5$; (c) $\mathrm{Re}=5\times10^5$. Panel (d) is the analog of panel (c) for the nonuniform shear flow at $\mathrm{Re}=5\times10^5$. In each panel, the neutral contours $(\omega_i=0)$ along with a few positive growth rate $(\omega_i>0)$ contours are shown.

flow in Fig. 2(d). Comparing the contours of positive growth rates in Figs. 2(c) and 2(d), we find that the maximum growth rate in the uniform shear flow can be larger by an order of magnitude.

Figure 3(a) shows the variation of the most unstable mode with α at a Mach number of $M=15$, with other parameters as in Fig. 2(c). The solid line denotes the growth rate (ω_i) and the dashed line the phase speed $(c_{ph}\equiv c_r=\omega_r/\alpha)$. It is observed that the flow is stable for low α, but becomes unstable at $\alpha\approx1.65$, with the corresponding phase speed crossing *zero* which implies that this instability belongs to the *mode II* [see Fig. 1(b)]; the flow becomes stable again for large enough α (>6.2). (Below $\alpha<1.65$, mode I is the least-stable mode for which $c_{ph}>1$, and hence the phase speed changes abruptly at $\alpha\approx1.65$.) Three peaks on the growth rate curve in Fig. 3(a) correspond to three distinct instability loops in Fig. 2(c). It is observed that the phase speed changes smoothly across the kinks on the growth-rate curve for $\alpha>1.65$, implying that there is no "mode crossing" across these apparent kinks. Hence, all three unstable peaks belong to the same mode (see following paragraph), and, according to the above mode classification, the origin of this instability is mode II. The effect of Reynolds numbers on the most unstable mode is shown in Fig. 3(b), with parameter values as in Fig. 3(a). It is observed that increasing the value of Re from 5×10^5 to 5×10^6, an additional unstable peak appears on the growth-rate curve near $\alpha=11$; however, the *dominant* instability (i.e., the mode having the maximum growth rate for all α for given Re and M) still comes from the *third peak* [that corresponds to the uppermost instability lobe in Fig. 2(c)], and this observation holds even at larger values of $\mathrm{Re}=5\times10^7$.

To find out whether the sharp peaks on the growth rate curves in Fig. 3 are bounded, we show the enlarged views of the first and third peaks [of Fig. 3(b)] in Figs. 4(a) and 4(b), respectively. It is clear that the growth rate varies *smoothly* across each peak, and the maximum growth rate at each peak is bounded; the *sharpness* of the first and third peaks in Fig. 3 is a consequence of large variation in growth rate (albeit smoothly) over a small range of α. Figure 4(c) shows the phase-speed variation corresponding to the third peak [i.e., Fig. 4(b)]; clearly, there is no discontinuity on the phase-speed curve, too. [The phase-speed variation across the first peak in Fig. 4(a) is also smooth, not shown.] These results suggest that the instability in Fig. 3 belongs to the same mode and the maximum growth rate at each peak remains bounded.

From the zoom of the first peak, as shown in Fig. 4(a), we observe that the peak height diminishes with increasing Re—this is a *viscous instability* since it disappears in the inviscid limit. On the other hand, the height of the second, flatter, peak in Fig. 3(a) increases with increasing Re that eventually approaches the asymptotic results on the *inviscid* mode-II instability of Duck *et al.* [19]. The effect of Re on the third peak in Fig. 3(a) can be ascertained from its enlarged version in Fig. 4(b). This instability becomes stronger with increasing Re, implying that this is an *inviscid* instability, too. It may be noted that this inviscid instability was not reported in Ref. [20] for the nonuniform shear flow.

Figure 5(a) shows the zoom of the left-hand corner of the stability map in Fig. 2(c). There are two narrow loops of instability at $M<4$. To find out the modal origin of these two instability loops, we plot, in Fig. 5(b), the variations of the growth rate (solid line) and the phase speed (dashed line) of

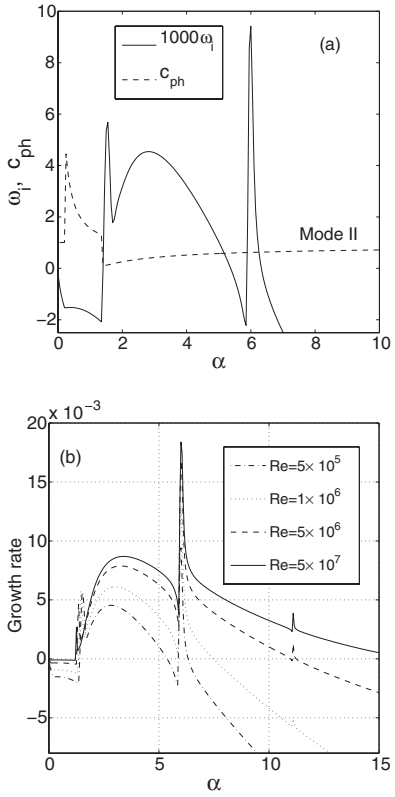

FIG. 3. (a) Variations of the growth rate (ω_i) and the phase speed (c_{ph}) of the most unstable mode with α for two-dimensional perturbations (β=0) and M=15; other parameters as in Fig. 2(c). (b) Effects of Reynolds number Re on the growth rate of the most unstable mode with α for β=0 and M=15.

the least-stable mode with α at M=3. From the variation of the phase speed c_{ph}, we find that the first unstable peak is due to the mode II (phase speed near zero) and the second peak due to the mode I (phase speed near unity). Therefore, the upper "narrow" instability loop in Fig. 5(a) belongs to mode I and the lower loop to mode II.

To find out the *dominant* instability mode over all α in Fig. 5(a), we plot the variation of the maximum growth rate

$$\omega_i^d = \max_{\alpha} \omega_i, \tag{14}$$

with M in Fig. 6(a), which increases monotonically with increasing M for the range of M shown (in fact, ω_i^d decreases beyond a critical value of M, see Fig. 2). It is clear from the phase-speed variation in Fig. 6(a) that there is no "mode crossing" and mode II remains the dominant instability for all M. This conclusion is in contrast to the result of Hu and Zhong [20] (for nonuniform shear flow) who found that the mode I remains the dominant mode at *small M* and the mode II at *moderate-to-large M*, as it is evident from Fig. 6(b). For the nonuniform shear flow, the range of M over which mode I remains the dominant mode increases marginally with Reynolds number (not shown for brevity). For example, at Re $=5\times10^7$, mode I is the dominant mode for $M\sim(1.5-3)$ and mode II for $M>3$.

The effect of *three-dimensional* perturbations on the least

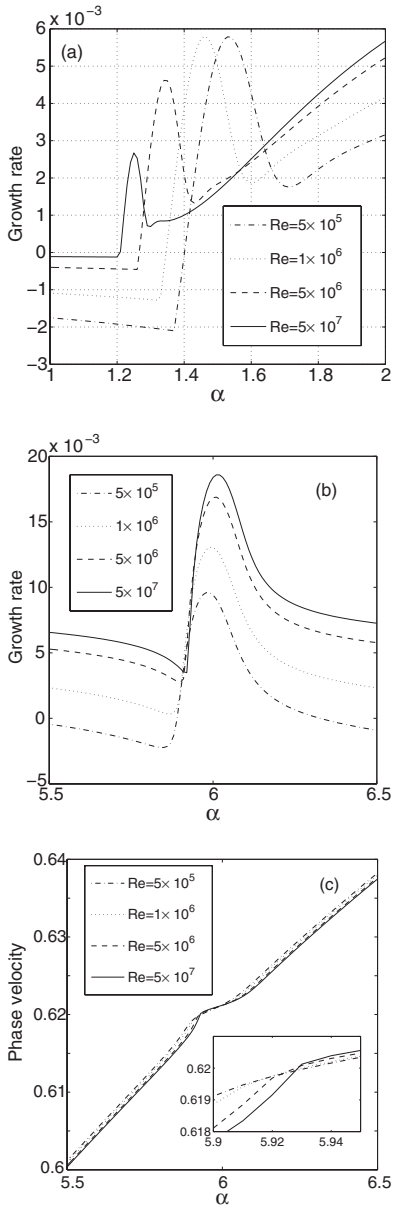

FIG. 4. (a) Enlarged view of the first peak of Fig. 3(b) around $\alpha\sim1.5$. (b) Enlarged view of the third peak of Fig. 3(b) around $\alpha\sim6$. (c) Variation of the phase-speed curve corresponding to the growth rates in panel (b).

stable growth rate is shown in Fig. 7(a) for different spanwise wave number β, with parameter values Re$=5\times10^5$ and M=15; the zoom of the third peak is displayed in Fig. 7(b). Comparing different growth-rate curves with the one for two-dimensional perturbations (β=0), we find that there is a window of α, slightly beyond the third peak, over which the three-dimensional perturbations are more unstable than their two-dimensional counterparts. Therefore, in general, Squire's theorem is not valid for the present flow configuration. This finding is in variance with the previous work [21] that Squire's theorem holds irrespective of the value of α in the uniform shear flow of an "isothermal" compressible fluid.

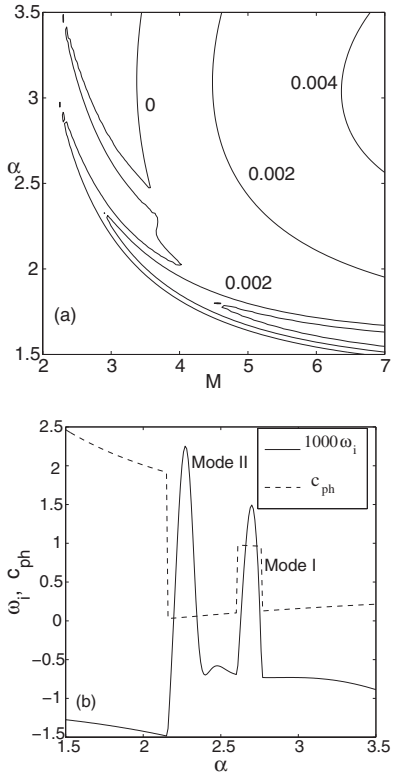

FIG. 5. (a) An expanded view of the stability map in Fig. 2(c) for low Mach numbers. (b) Variations of the most unstable mode with α at $M=3$.

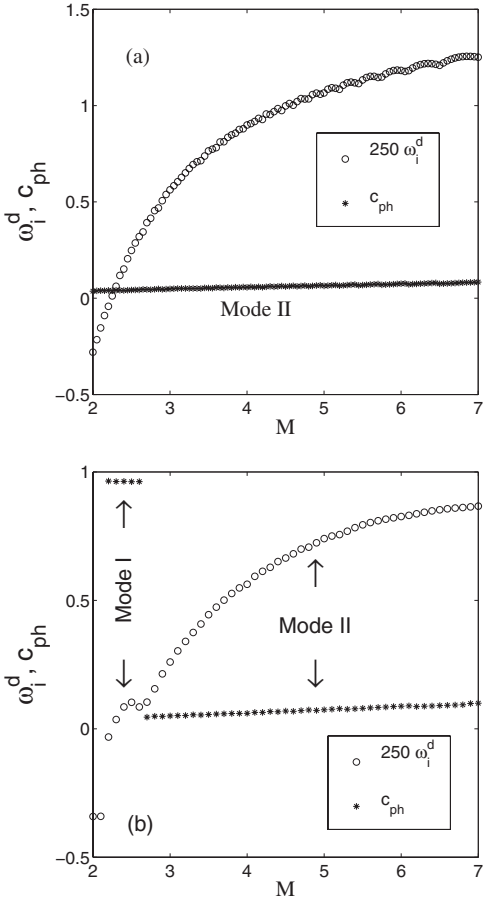

FIG. 6. Variations of the maximum growth rate over all α, ω_i^d, and the corresponding phase speed, c_{ph}, with M at $\mathrm{Re}=5\times10^5$: (a) uniform shear; (b) nonuniform shear. The arrows in panel (b) are used to identify the portions of ω_i^d and c_{ph} over M for both mode I and mode II.

C. Critical Reynolds number

Figures 8(a) and 8(b) show the contours of the least stable growth rate in the (Re,α) plane for two-dimensional disturbances ($\beta=0$) with $M=3$ and $M=5$, respectively. The upper and lower instability loops in Fig. 8(a) correspond to mode-I and mode-II instability, respectively, whereas the instability loop in Fig. 8(b) arises solely from mode II. For $M=3$, the flow becomes unstable to *mode I* at $(\mathrm{Re},\alpha)\approx(123\,900, 2.835)$, and to *mode II* at $(\mathrm{Re},\alpha)\approx(50\,060, 2.545)$. Therefore, the critical Reynolds number (Re_{cr}) at which the instability sets in *first* is determined by *mode II*—this observation holds at other values of M [except at low M, see Fig. 6(b)]. A comparison of the values of Re_{cr} and α_{cr} between the uniform and nonuniform shear flows is given in Table I for different Mach numbers. It is clear that the critical Reynolds number for the uniform shear flow is significantly smaller than that for its nonuniform counterpart; for example, at $M=10$, Re_{cr} of two mean flows differ by a factor of 5.6. Therefore, we conclude that *the viscosity stratification of the base flow would lead to a "delayed" transition in compressible Couette flow in terms of modal instability*. Another interesting observation in Table I is that the variation of Re_{cr} with M is *nonmonotonic* in the sense that the critical Reynolds number reaches a minimum at some intermediate value of Mach number.

The effect of Reynolds number on mode-I instability [upper loops in Figs. 5(a) and 8(a)] is to make it a *neutral* mode in the inviscid limit as is the case for nonuniform shear flow [19]. This effect is similar to the first-peak mode-II instability in Fig. 4(a) where the viscosity plays a destabilizing role. Therefore, while the viscosity plays a *dual* role of destabilizing [at small α as in Fig. 4(a)] and stabilizing [at moderate-to-large α as in Fig. 4(b)] the mode-II instability, it destabilizes the mode-I instability. This conclusion also holds for the nonuniform shear flow [20].

Even though we have presented all stability results on mode-I and mode-II instabilities, it may be noted that the higher-order even (IV,…) and odd (III,…) inviscid modes can also become unstable, but they remain *subdominant* with respect to mode-II instability.

D. Energy analysis: Instability mechanism

The exponential instability can be understood by considering the rates of transfer of energy by the different terms in the momentum and thermal equations. For this we need to define a suitable norm of the perturbations which can represent the energy. We define the perturbation energy density as

$$\mathcal{E}(\alpha,\beta,t)=\int_0^1 \tilde{\mathbf{q}}^{\dagger}(y,t)\mathcal{M}\tilde{\mathbf{q}}(y,t)dy, \tag{15}$$

where the superscript † on any quantity refers to its conjugate value, and the weight matrix $\mathcal{M}$ is diagonal and positive

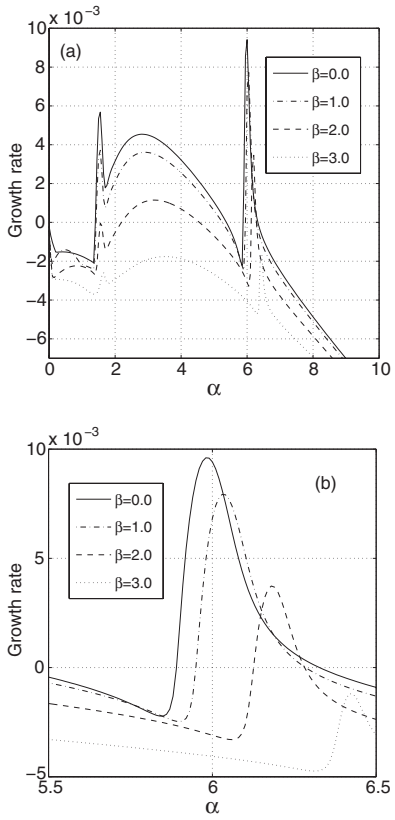

FIG. 7. (a) Variations of the growth rate (ω_i) of the most unstable mode with α for various values of the spanwise wave number β with $\mathrm{Re}=5\times10^5$ and $M=15$. (b) Zoom of panel (a) around the third peak.

definite. Among various choices of the weight matrix $\mathcal{M}$, we consider the following:

$$\mathcal{M} = \mathrm{diag}\{\rho_0, \rho_0, \rho_0, T_0/\rho_0\gamma M^2, \rho_0/\gamma(\gamma-1)T_0M^2\}, \quad (16)$$

which corresponds to the well-known Mack norm [22] that has been used in many transient growth studies on compressible flows [8,18]. A special property of this norm is that this definition of energy is free from any contribution due to the pressure related terms in the governing equations.

Equation (15) can be written for the least decaying mode, which has an exponential time dependence, as

$$\mathcal{E}_{ld}(\alpha,\beta,t) = \exp[2\ \mathrm{Im}(\omega_{ld})t]\int_0^1 \mathbf{q}'^{\dagger}_{\mathbf{ld}}(y)\mathcal{M}\mathbf{q}'_{ld}(y)dy, \quad (17)$$

where the subscript "*ld*" refers to "least-decaying" mode. The rate of change of this energy with respect to time can be written as

$$\frac{\partial\mathcal{E}_{ld}}{\partial t} = 2\ \mathrm{Im}(\omega_{ld})\exp[2\ \mathrm{Im}(\omega_{ld})t]\int_0^1 \mathbf{q}'^{\dagger}_{\mathbf{ld}}(y)\mathcal{M}\mathbf{q}'_{\mathbf{ld}}(y)dy, \quad (18)$$

which can be manipulated using Eq. (12) to yield

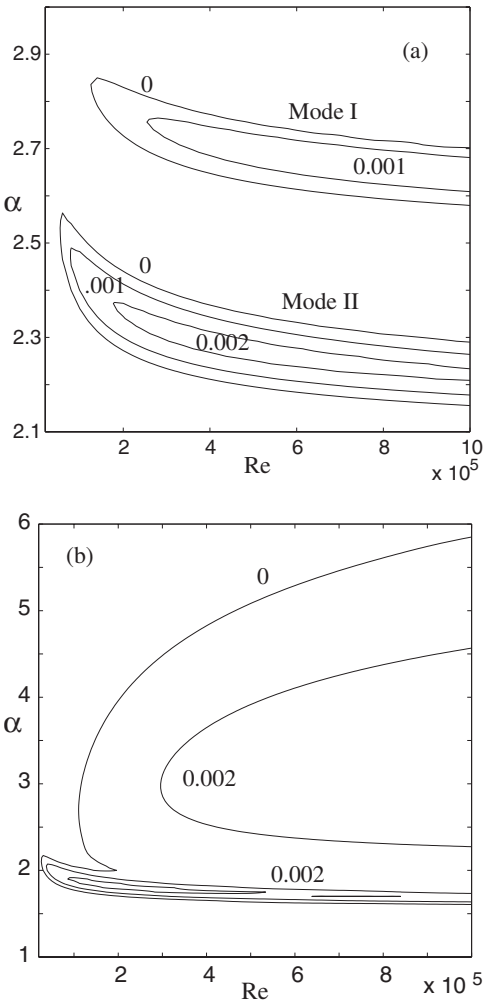

FIG. 8. Stability maps for uniform shear flow in the (Re,α) plane for two-dimensional ($\beta=0$) perturbations: (a) $M=3$; (b) $M=5$. In each panel, the neutral contours ($\omega_i=0$) along with a few positive growth rate ($\omega_i>0$) contours are shown.

$$\frac{\partial\mathcal{E}_{ld}}{\partial t} = -i\exp[2\ \mathrm{Im}(\omega_{ld})t]\int_0^1 \mathbf{q}'^{\dagger}_{\mathbf{ld}}(y)\mathcal{M}\mathcal{L}\mathbf{q}'_{\mathbf{ld}}(y)dy + \mathrm{c.c.} \quad (19)$$

Now, we decompose the total energy-transfer rate into those coming and going through different physical routes.

TABLE I. Critical stability parameters for $\beta=0$.

	Uniform shear		Nonuniform shear	
Mach number	Re_{cr}	α_{cr}	Re_{cr}	α_{cr}
$M=3$	50 060	2.545	1 64 900	2.840
$M=5$	23 830	2.130	85 725	2.570
$M=10$	45 040	1.870	2 52 700	2.485
$M=15$	85 150	1.810	6 55 850	2.490

$$\frac{\partial \mathcal{E}_{ld}}{\partial t} = \exp[2\ \mathrm{Im}(\omega_{ld})t]\sum_{j=0}^{4} \dot{\mathcal{E}}_j, \tag{20}$$

where the explicit forms of the $\dot{\mathcal{E}}_j$'s are given in the Appendix. $\dot{\mathcal{E}}_0$ is the energy-transfer rate due to the convection by mean flow, $\dot{\mathcal{E}}_1$ is the same from the mean flow to the perturbation, $\dot{\mathcal{E}}_2$ is due to viscous dissipation, $\dot{\mathcal{E}}_3$ is due to the thermal diffusion, and finally $\dot{\mathcal{E}}_4$ is due to the viscous dissipation term in the thermal energy equation.

Note that the above expressions involve the eigenfunction of the least-stable mode and its derivative. The numerical estimation of these quantities is a challenging one for the least-decaying mode at high Re and M with large α and β. The streamwise velocity and temperature perturbations exhibit boundary-layer-like steep variations near the wall. These variations are extremely rapid at high α. Moreover, at high α there are also internal layers. An accurate estimation of the above quantities will require a highly resolved scheme to capture these steep variations. Therefore we used a multidomain spectral calculation, with appropriate matching conditions which can be found in [23,24] except that we have relaxed the matching of the derivative of the density perturbation, since the highest order of density is one in the continuity equation. A check on the accuracy of the results has been made by estimating the energy transferred by the pressure terms which must be vanishingly small by the definition of the Mack energy norm.

Figure 9 shows the rates of different constituent energies routed via different physical processes at $M=5$ for $\mathrm{Re}=4\times10^5$. In this figure, $\dot{\mathcal{E}}_4$ is not shown since it is negligibly small. Figure 9(a) shows results for two-dimensional (2D) modes for a range of α. The sudden changes for $1.5<\alpha<2$ is due to a mode crossing. The energy transferred from the mean flow plays a dominant role for the onset of instability. The viscous dissipation and thermal diffusion plays the role of routing the energy out of perturbations; it is interesting to note that the thermal diffusion rate is dominant over the rate of viscous dissipation for 2D modes. Figure 9(b) shows these energy transfer rates for 3D modes for a range of β with $\alpha=3$. The main difference is that at high values of β the viscous dissipation dominates over thermal dissipation for 3D modes. This observation holds at other values of M and Re.

As shown in Fig. 8(a) there are distinct regions of instabilities in the $(\mathrm{Re}-\alpha)$ plane due to mode I and mode II. In order to study the characteristics special to each of these modes, we show the budget of energy-transfer rates across a range of α spanning two different regions of instabilities in Fig. 10, with parameter values as in Fig. 8(a). Both mode I and mode II instability regions exhibit a qualitatively similar behavior in the shares of each physical processes, except that the balancing involved is quantitatively different for each mode. For mode-I instability, the energy-transfer rate from the mean flow and the thermal-diffusion rate are much larger than those for mode II.

The distinction between mode-I and mode-II instability becomes clearer when we look at the distribution of different perturbation energies across y. Figure 11 shows this distribution for $\alpha=2.75$ [which belongs to mode I in Fig. 8(a)], and Fig. 12 shows the same for $\alpha=2.3$ (which belongs to mode II). These figures show that the energy-transfer rate from mean flow occurs close to the moving and isothermal top wall for mode I, whereas it occurs in the bulk of the flow domain for mode II. As one expects the viscous dissipation is culminated near the walls. This is more at the lower wall for mode I, and at the upper wall for mode II. Both modes exhibit a larger loss-by-conduction near the top wall. This is because the temperature gradient is set to zero at the lower wall via the adiabatic boundary condition. The heat gener-

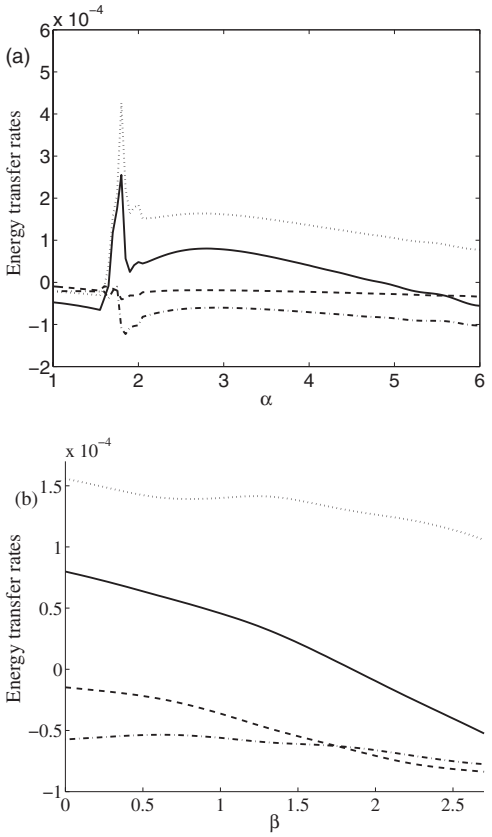

FIG. 9. Rates of transfer of different energies [$\mathcal{E}_i$, see Eq. (20)] for $\mathrm{Re}=4\times10^5$ at $M=5$. Solid line, total energy-transfer rate; dashed line, viscous dissipation; dotted line, from base flow; dash-dotted line, thermal diffusion. (a) $\beta=0$; (b) $\alpha=3$.

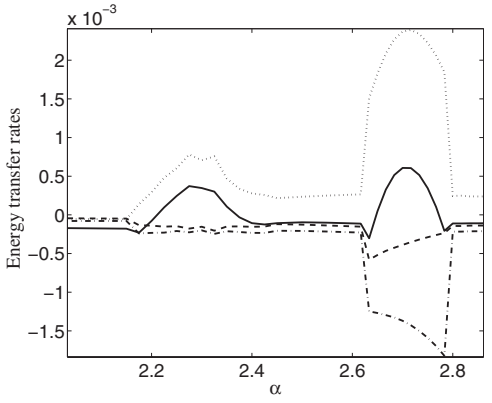

FIG. 10. Same as Fig. 9(a), but for $M=3$.

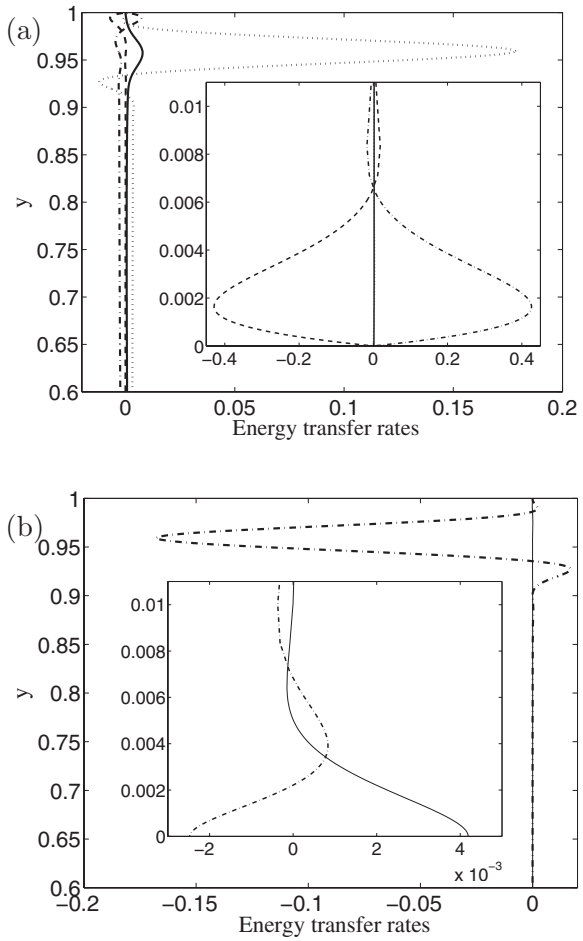

FIG. 11. Energy-transfer rates, $\mathcal{E}_i$, vs y for $\alpha=2.75$, $\beta=0$, and $\mathrm{Re}=4\times10^5$ at $M=3$. (a) Solid line, rate of total energy; dashed line, viscous dissipation; dashed-dotted line, transferred by pressure terms; dotted line, rate of transfer from mean flow. (b) Solid line, rate of heat produced by friction; dashed-dotted line, thermal diffusion rate. Insets in each panel show them at close to the lower wall.

ated due to viscous dissipation is more near the lower wall for mode I and higher near the upper wall for mode II. This is in accordance with the momentum loss due to viscous dissipation for both modes. Finally, apart from the constituent energy-transfer rates found in the Appendix, Figs. 11 and 12 also show the local energy-transfer rates by pressure. The expression for this quantity, say, $\dot{\mathcal{E}}_5(t,y)$, is

$$\dot{\mathcal{E}}_5(t,y) = -\frac{\exp[2\ \mathrm{Im}(\omega_{ld})t]}{\gamma M^2}(p'^{\dagger}Dv' + v'^{\dagger}Dp') + \text{c.c.} \tag{21}$$

Though this quantity does not contribute to the overall total energy-transfer rate (since this quantity vanishes upon integration across the channel width), it plays a role in the distribution of the same across the channel width.

IV. TRANSIENT ENERGY GROWTH

Let us write the linear stability equations in an evolution form

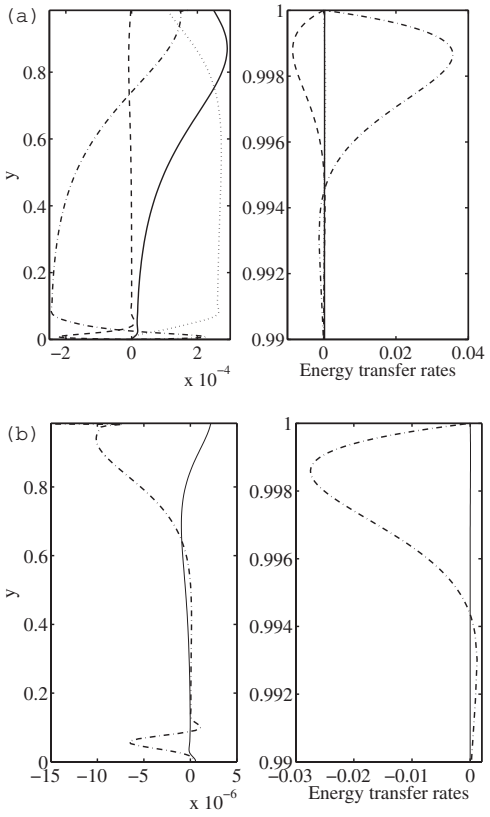

FIG. 12. Same as Fig. 11, but for $\alpha=2.3$. The subplots on the right show energy-transfer rates near the upper wall.

$$\frac{\partial\tilde{\mathbf{q}}}{\partial t} = -i\mathcal{L}\tilde{\mathbf{q}}, \tag{22}$$

where $\tilde{\mathbf{q}}(y,t;\alpha,\beta)$ is the inverse Fourier transform of $\hat{\mathbf{q}}(x,y,z,t)$; the elements of the linear operator, $\mathcal{L}$, are omitted for sake of brevity. In contrast to the *modal* linear stability analysis that deals with the long-time dynamics of any system via the normal-mode approach, the key idea of the *nonmodal* analysis is to probe the short-time dynamics of the system in terms of perturbation energy in the parameter space where the flow is *stable* (such as in Fig. 2) according to the linear stability analysis, and investigate the potential of such stable flows to *amplify* the initial perturbation energy.

Let $G(t,\alpha,\beta;\mathrm{Re},M)$ be the maximum possible energy amplification at any time t, i.e.,

$$G(t,\alpha,\beta;\mathrm{Re},M) \equiv G(t) = \max_{\tilde{\mathbf{q}}(\mathbf{0})}\frac{\mathcal{E}(\alpha,\beta,t)}{\mathcal{E}(\alpha,\beta,0)}, \tag{23}$$

where $G(t)$ is optimized over all initial conditions which is computed using the singular value decomposition. For an efficient computation of $G(t)$, only a selected portion of the spectra (see Fig. 1) is chosen [18], corresponding to the modes whose phase speeds are within the range $-1<\omega_r/\alpha<2$ (i.e., comparable to the extremes of the mean-flow velocity which varies between 0 and 1), and the decay rate is less than 0.5 (i.e., $\omega_i>-0.5$). With this choice of modes, the number of selected modes K [$\ll 5N$, where $(N+1)$ is the number of collocation points] can be reduced by a factor of 5

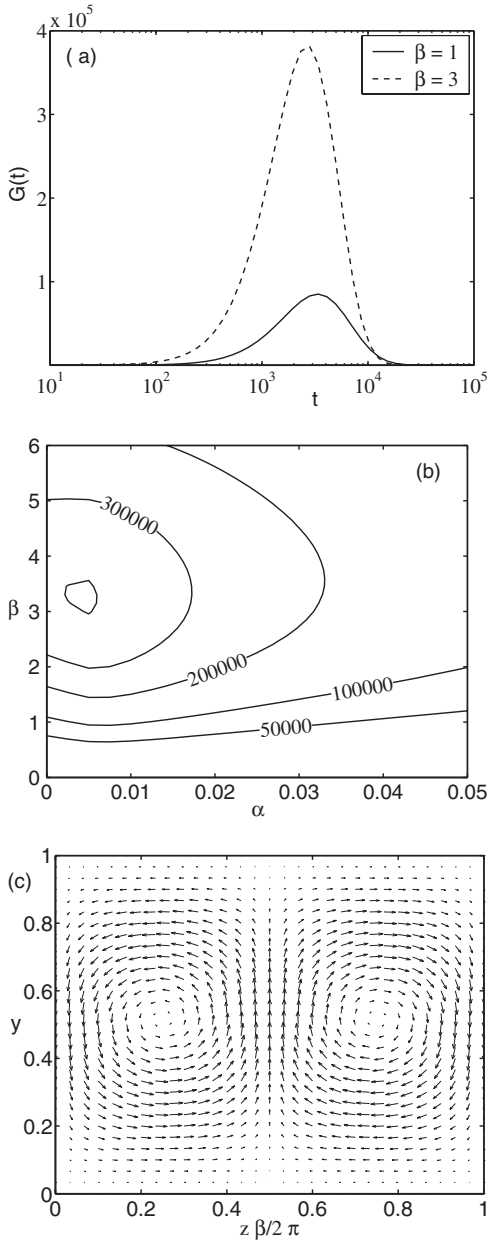

FIG. 13. (a) Variation of the energy amplification factor, $G(t)$, with time for parameter values of $\mathrm{Re}=10^5$, $M=2$, and $\alpha=0$. (b) Contours of $G_{\max}$ in the (α,β) plane for $\mathrm{Re}=10^5$ and $M=2$. (c) Pattern of optimal perturbation velocities at $t=0$ in the (z,y) plane for $\alpha=0$, $\beta=3$, $M=2$, and $\mathrm{Re}=10^5$.

or more. The related details on numerical scheme are documented in our earlier paper [18].

A. Results on energy growth and optimal perturbations

The variation of $G(t,\alpha,\beta)$ with time for uniform shear flow is shown in Fig. 13(a) for different spanwise wave number β, with $\mathrm{Re}=10^5$, $M=2$, and $\alpha=0$; the solid and dashed lines correspond to $\beta=1$ and 3, respectively. It is observed that the initial energy density can be amplified by a factor of 10^5 or more over a time scale of order $t=O(10^3)$ for both β; in the long-time limit $(t\to\infty)$, $G(t)$ decays to zero since the flow is stable. Figure 13(b) shows the contours of the maximum amplification of energy over all time [that occurs at $t=t_{\max}$ such as in Fig. 13(a)] in the (α,β) plane,

$$G_{\max}(\alpha,\beta;\mathrm{Re},M)=\max_{t\geq 0}G(t,\alpha,\beta;\mathrm{Re},M) \tag{24}$$

for $\mathrm{Re}=10^5$ and $M=2$. It is seen that larger energy amplification occurs for smaller values of streamwise wave number. For the dash line in Fig. 13(a), the *optimal* velocity patterns in the (y,z) plane at $t=0$ is shown in Fig. 13(c). [The velocity pattern at $t=t_{\max}$ looks similar to that in Fig. 13(c).] This represents a pure streamwise vortex which is typical of all shear flows [4,5,18]. The structural features of optimal patterns in compressible uniform shear flow look similar to those in incompressible shear flows.

The global maximum of $G_{\max}$ over all combinations of wave number (α,β),

$$G_{\mathrm{opt}}(\mathrm{Re},M)=\sup_{\alpha,\beta}G_{\max}(\alpha,\beta;\mathrm{Re},M), \tag{25}$$

is called the *optimal energy growth* G_{opt} that occurs at $(t_{\mathrm{opt}},\alpha_{\mathrm{opt}},\beta_{\mathrm{opt}})$. The variations of G_{opt} and the corresponding optimal time t_{opt}, with Mach number M, are shown in Figs. 14(a) and 14(b). The solid and dashed lines in each panel correspond to the uniform and nonuniform shear flow, respectively; $\mathrm{Re}=10^5$ for these plots. Both G_{opt} and t_{opt} decrease monotonically with increasing M. The magnitude of G_{opt} is much larger for the uniform shear flow; the optimal time t_{opt} is also larger by a factor of 2 or more, implying that the energy growth can be sustained over a longer duration in uniform shear flow. These overall observations on transient energy growth hold at other subcritical values of M and Re. Therefore, the uniform shear flow is more susceptible to subcritical transitions than its nonuniform counterpart. As in the case of modal instability in Sec. III C, we can conclude that *the viscosity stratification along with nonuniform shear would also lead to a "delayed" subcritical transition in compressible Couette flow in terms of nonmodal instability*.

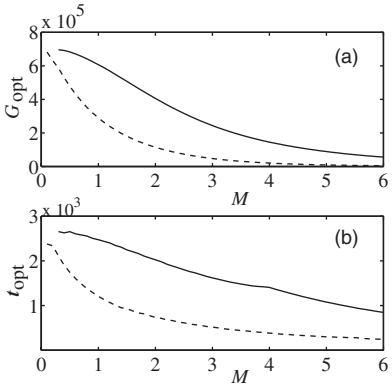

FIG. 14. Variations of (a) the optimal energy growth G_{opt}, (b) optimal time t_{opt} with Mach number M for $\mathrm{Re}=10^5$. The solid line correspond to the uniform shear mean flow, and the dashed line to nonuniform shear.

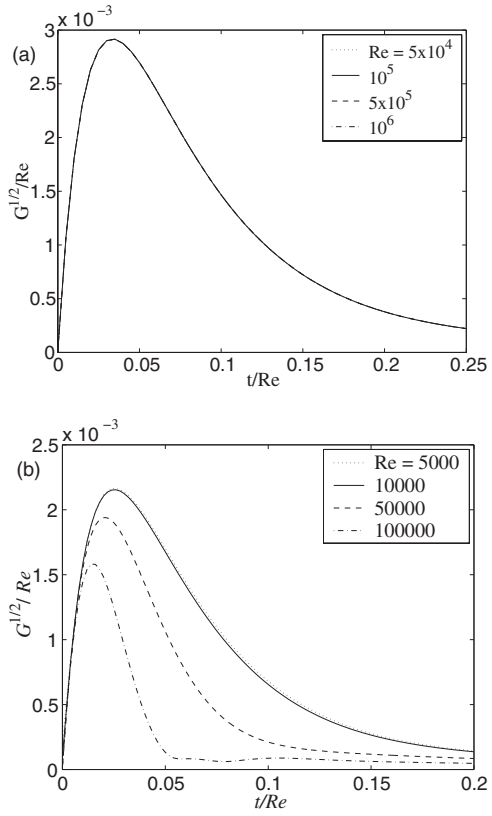

FIG. 15. Verification of the quadratic scaling law for $G(t)$ for streamwise-independent ($\alpha=0$) perturbations with $\beta=1.0$ and $M=2$: (a) Uniform shear; (b) nonuniform shear.

B. Scalings of $G_{\max}$ and $t_{\max}$

In a recent paper [18], we have shown that the well-known scaling law of incompressible shear flows [3], $G_{\max}$, *varies quadratically with the Reynolds number* Re, *and* $t_{\max}$ *varies linearly with* Re *for streamwise-independent* ($\alpha=0$) *modes*, does not hold for the nonuniform shear compressible Couette flow. To check the validity of this scaling law for the present uniform shear flow, we have plotted in Fig. 15(a) the variations of the rescaled energy growth $\sqrt{G(t)}/\mathrm{Re}$ with rescaled time t/Re for four different Reynolds number at $M=2$ and $\beta=1.0$; the corresponding plot for the nonuniform shear flow is displayed in Fig. 15(b). (Plots for different β look similar and hence not shown.) It is clear that the quadratic scaling of $G_{\max}$ with Re holds for the uniform shear case but does not hold for its nonuniform shear counterpart.

For the *nonuniform shear flow*, we have argued [18] that the following terms, associated with density and temperature fluctuations, in the y- and z-momentum equations,

$$\mathcal{L}_{24} = -i\left(T_{0y} + T_0\frac{d}{dy}\right) \Big/ \rho_0\gamma M^2, \quad \mathcal{L}_{34} = \beta T_0^2/\gamma M^2,$$

$$\mathcal{L}_{25} = -i\left(\rho_{0y} + \rho_0\frac{d}{dy}\right) \Big/ \rho_0\gamma M^2, \quad \mathcal{L}_{35} = \beta/\gamma M^2, \quad (26)$$

are responsible for the violation of the above quadratic scaling-law since setting them to zero, $\mathcal{L}_{24}=\mathcal{L}_{25}=\mathcal{L}_{34}=\mathcal{L}_{35}=0$, the rescaled energy-growth curves for different Re collapses onto a single curve. Interestingly, for the *uniform shear flow*, too, the above terms $\mathcal{L}_{24}$, $\mathcal{L}_{25}$, $\mathcal{L}_{34}$, and $\mathcal{L}_{35}$ remain *nonzero*, but *the quadratic scaling still holds*. In this paper, we resolve this apparent contradiction via the following analysis of the linear operator in conjunction with the Mack transformation.

Let us rewrite the linear stability equation (22) as

$$\frac{\partial\tilde{\mathbf{q}}}{\partial t} = -i\mathcal{L}^q\tilde{\mathbf{q}} - i\mathcal{L}^p\tilde{\psi}, \quad (27)$$

where

$$\mathcal{L}^p_{ij} = \mathcal{L}_{(i+1)(j+3)} \quad \text{for } i=1,2;\ j=1,2, \quad (28)$$

$$\mathcal{L}^q = \mathcal{L} \quad \text{with } \mathcal{L}^q_{ij}=0 \quad \text{for } i=2,3;\ j=4,5, \quad (29)$$

$$\tilde{\phi}=\{\tilde{v},\tilde{w}\} \quad \text{and} \quad \tilde{\psi}=\{\tilde{\rho},\tilde{T}\}. \quad (30)$$

Note that the operator $\mathcal{L}^p$ comes from y and z-momentum equations, with elements as in Eq. (22). Under the Mack transformation [22], $\{\tilde{u},\tilde{\phi},\tilde{\psi},t\}\rightarrow\{\mathrm{Re}\,\bar{u},\bar{\phi},\mathrm{Re}\,\bar{\psi},\mathrm{Re}\,\bar{t}\}$, Eq. (27) transforms into

$$\frac{\partial\bar{\mathbf{q}}}{\partial\bar{t}} = -i\bar{\mathcal{L}}\bar{\mathbf{q}} - i\,\mathrm{Re}^2\,\mathcal{L}^p\bar{\psi}, \quad (31)$$

where $\bar{\mathcal{L}}$ is independent of Re and $\bar{\mathbf{q}}=(\bar{u},\bar{\phi},\bar{\psi})^T$. In terms of these barred variables, an evolution equation for the total perturbation energy density (15) can be derived as

$$\frac{\partial\bar{\mathcal{E}}}{\partial\bar{t}} = -i\int_0^1\bar{\mathbf{q}}^\dagger\mathcal{M}\bar{\mathcal{L}}\bar{\mathbf{q}}dy - i\,\mathrm{Re}^2\int_0^1\rho_0\bar{\boldsymbol{\phi}}^\dagger\mathcal{L}^p\bar{\psi}dy + \text{c.c.}, \quad (32)$$

where c.c. represents complex conjugate terms. This equation can be integrated with respect to $\bar{t}$ to yield

$$\bar{\mathcal{E}}(\bar{t}) = \bar{E}(\bar{t}) + \mathrm{Re}^2\,\bar{\mathcal{E}}_p(\bar{t}), \quad (33)$$

where $\bar{E}(\bar{t})$ is the first term in Eq. (32) integrated with respect to $\bar{t}$, and the second term, $\bar{\mathcal{E}}_p(\bar{t})$, represents the energy associated with operator $\mathcal{L}^p$. If we divide $\mathcal{L}^p$ by Re^2 in Eq. (31), then Eq. (33) becomes independent of Re, and hence we expect the scaling of $G(t)$ to hold.

The above analysis is verified in Fig. 16 where the energy growth curves for different Reynolds numbers are seen to collapse on a single curve for the rescaled operator $\mathcal{L}^p\rightarrow\mathcal{L}^p/\mathrm{Re}^2$ in Eq. (31).

It is interesting to note in Fig. 15(b) that the scaling $G(t)\sim\mathrm{Re}^2$ holds at low Reynolds numbers ($\mathrm{Re}\leq10^4$) even for the nonuniform shear flow, and hence the contribution of $\mathcal{L}^p$ to the perturbation energy must be negligible for such low Re. The latter statement can be confirmed if we explicitly compute the contribution of energy due to $\mathcal{L}^p$. Let us express the total energy density $\mathcal{E}(t)$ as

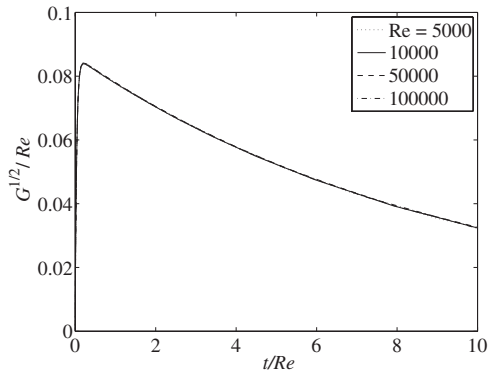

FIG. 16. Variation of $\sqrt{G}/\mathrm{Re}$ with time by rescaling the operator $\mathcal{L}^p \to \mathcal{L}^p/\mathrm{Re}^2$ in Eq. (31), with parameters as in Fig. 15(b).

$$\mathcal{E}(t) = \sum_{l,k} c_l^\dagger c_k \frac{\exp[-\mathrm{i}(\omega_k - \omega_l^\dagger)t]}{\omega_k - \omega_l^\dagger} \int_0^1 \mathbf{q_l}'^\dagger \mathcal{M}\mathcal{L}\mathbf{q_k}' dy + \mathrm{c.c.}, \tag{34}$$

where c_k's are the expansion coefficients of $\tilde{\mathbf{q}}$,

$$\tilde{\mathbf{q}}(y,t) = \sum_k c_k \exp[-i\omega_k t]\mathbf{q_k}'(y), \tag{35}$$

which can be evaluated by the singular value decomposition of the propagator of $\tilde{\mathbf{q}}$ such that $\mathcal{E}(t_{\max}) = G_{\max}$. In Eq. (34), the eigenfunction $\mathbf{q}'$ is normalized [to make the initial total energy $\mathcal{E}(0)=1$] with respect to the weight matrix $\mathcal{M}$, such that $\|\tilde{\mathcal{M}}\mathbf{q_k}'\| = 1$, where $\tilde{\mathcal{M}}$ is given by $\tilde{\mathcal{M}}^\dagger\tilde{\mathcal{M}} = \mathcal{M}$. It is straightforward to verify from Eq. (34) that the contribution of the terms in Eq. (26) to the total energy is

$$\mathcal{E}_p(t) = \sum_{l,k} c_l^\dagger c_k \frac{\exp[-i(\omega_k - \omega_l^\dagger)t]}{(\omega_k - \omega_l^\dagger)\gamma M^2} \times \int_0^1 [-iv_l'^\dagger Dp_k' + \beta w_l'^\dagger p_k']dy + \mathrm{c.c.} \tag{36}$$

Figure 17(a) shows the variation of $\mathcal{E}_p$ with time at a Reynolds number $\mathrm{Re}=10^5$; the symbols, circle, and triangle, correspond to times at which $G_{\max}$ occurs for nonuniform and uniform shear flows, respectively. It is seen that for the case of nonuniform shear $\mathcal{E}_p$ at $t=t_{\max}$ is much larger in comparison with that for uniform shear. At a low Reynolds number $\mathrm{Re}=10^4$, however, $\mathcal{E}_p(t_{\max})$ is negligible for both uniform and nonuniform shear flows [see Fig. 17(b)], and hence the scaling of $G(t)$ holds for relatively small Re [see Fig. 15(b)] in nonuniform shear flow.

The above analysis suggests that the (streamwise-independent) linear operator $\mathcal{L}$ of compressible flows can be partitioned into a Reynolds number dependent operator, $\mathcal{L}_p$, and a Reynolds number independent operator $\bar{\mathcal{L}}$ [Eqs. (27) and (31)]. The contribution of this Re-dependent operator, $\mathcal{L}_p$, to perturbation energy would decide whether the scaling $G_{\max} \sim \mathrm{Re}^2$ would hold or not for a given mean flow. For the uniform shear flow, $\mathcal{L}_p$ has negligible contribution to the energy growth and hence the quadratic scaling law holds.

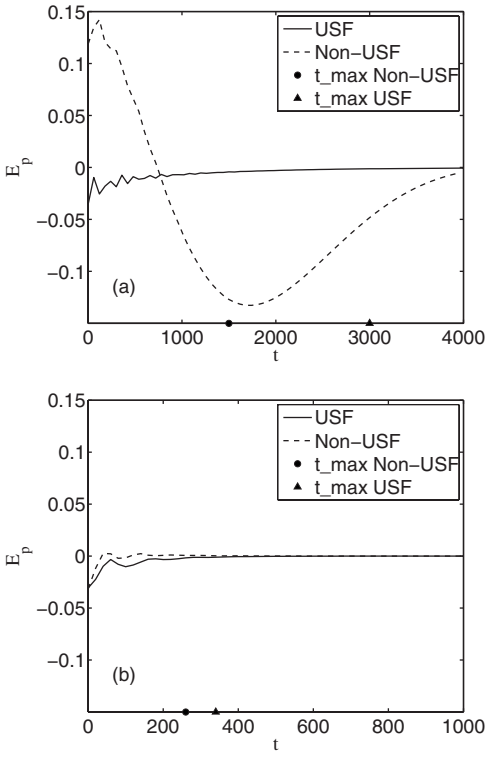

FIG. 17. Variation of $\mathcal{E}_p$ with time for uniform and nonuniform shear flows: $M=2$, $\beta=1$, and $\alpha=0$. (a) $\mathrm{Re}=10^5$ and (b) $\mathrm{Re}=10^4$.

C. Inviscid algebraic growth and optimal perturbation

The purely inviscid nature of the algebraic growth suggests one could try to obtain the transient growth characteristics directly from inviscid equations. As it has been shown numerically in the earlier section that the algebraic growth is very pronounced for the modes that are independent of the streamwise coordinate (i.e., $\alpha=0$). For such a unidirectional flow, Ellingsen and Palm [25] had found an analytical solution for incompressible flows. An extension of this solution for density and temperature perturbations was considered for the compressible situation [26] which resulted in a constraint due to the continuity equation which relates spanwise velocity with normal velocity. Further, this solution would also result in another constraint which relates density and temperature perturbations, which was not considered before, but is considered here [24]. The Ellingsen-Palm solution for compressible shear flow can be written as

$$\tilde{u}_{\mathrm{ivs}} = u'_{\mathrm{ivs}} - U_{0y}v'_{\mathrm{ivs}}t, \tag{37}$$

$$\tilde{v}_{\mathrm{ivs}} = v'_{\mathrm{ivs}}, \tag{38}$$

$$\tilde{w}_{\mathrm{ivs}} = \frac{i}{\beta}Dv'_{\mathrm{ivs}}, \tag{39}$$

$$\tilde{\rho}_{\mathrm{ivs}} = -\rho_0^2 T'_{\mathrm{ivs}} - \rho_{0y}v'_{\mathrm{ivs}}t, \tag{40}$$

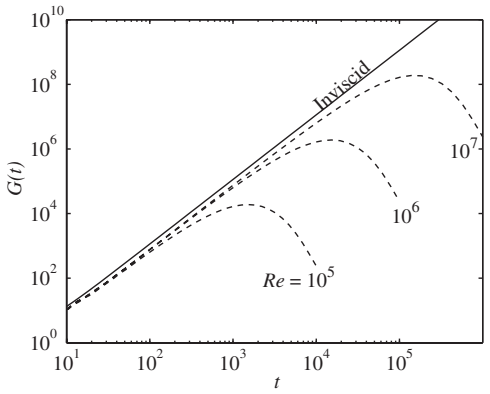

FIG. 18. Viscous and inviscid energy growth curves for $\beta=1$ and $M=5$. Solid line, inviscid solution, $\hat{G}(t)$; dashed line, full viscous solution, $G(t)$.

$$\tilde{T}_{\text{ivs}} = T'_{\text{ivs}} - T_{0y} v'_{\text{ivs}} t, \tag{41}$$

where u'_{ivs}, v'_{ivs}, and T'_{ivs} are the initial perturbation quantities which are to be determined via an optimization procedure; in the following analysis, the subscript "ivs," which refers to "inviscid solution," is dropped for the sake of simplicity. The perturbation energy $\mathcal{E}(t)$ can be written in the basis of the quantities u', v', and T', after removing w' and ρ' using the above-mentioned constraints, as

$$\mathcal{E}(t) = \int_0^1 \left(\rho_0 |\tilde{u}|^2 + \frac{\tilde{v}^\dagger}{\beta^2} [\rho_0(\beta^2 - D^2) - \rho_{0y} D] \tilde{v} + \frac{\rho_0^2}{(\gamma-1)M^2} |\tilde{T}|^2 \right) dy. \tag{42}$$

Let $\tilde{\psi}=\{\tilde{u},\tilde{v},\tilde{T}\}^T$ and $\psi'=\{u',v',T'\}^T$. Then the above equation can be written as

$$\mathcal{E}(t) = \int_0^1 \psi'^\dagger A^\dagger \hat{\mathcal{M}} A \psi' dy, \tag{43}$$

where $\hat{\mathcal{M}} = \text{diag}\{\rho_0, [\rho_0(\beta^2 - D^2) - \rho_{0y} D]/\beta^2, \rho_0^2/(\gamma-1)M^2\}$, and A is a 3×3 matrix which can be defined by casting Eqs. (37), (38), and (41) in the form $\tilde{\psi}=A\psi'$. Now $\hat{G}(t) \equiv \max_{\psi'} \mathcal{E}(t)$ is given by

$$\hat{G}(t) = \max(\{\lambda_k\}), \tag{44}$$

where λ_k's are the eigenvalues of the differential equation

$$A^\dagger \hat{\mathcal{M}} A \psi' = \lambda \hat{\mathcal{M}} \psi' \tag{45}$$

with the boundary conditions $v'(0)=v'(1)=0$. In contrast to Hanifi and Henningson's [26] four-variable model, this equation (45) has only three dependent variables and hence called a "reduced" model. The constraint of vanishing pressure fluctuation is essential to obtain this reduced model; the related spatial problem has been solved elsewhere [24].

Equation (45) has been solved using the spectral method. Figure 18 shows the inviscid algebraic growth curve $\hat{G}(t)$ at $M=5$ and $\beta=1$. The viscous transient growth curves are also shown for three different Reynolds numbers. It is seen that for the entire growth duration the viscous and inviscid growths agree quantitatively, demonstrating the inviscid nature of the algebraic growth. In terms of energy-transfer rate, only the following term (see the Appendix)

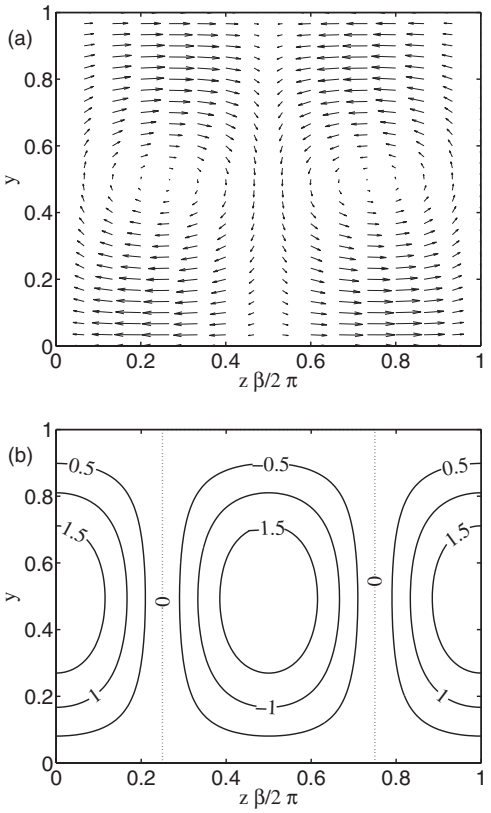

FIG. 19. Inviscid optimal patterns of velocity fluctuations given by Eq. (45) for $M=5$ and $\beta=1$. (a) Velocities in y-z plane; (b) contours of $\tilde{u}$.

$$\dot{\mathcal{E}}(t) = -\int_0^1 \left[\rho_0 U_{0y} \tilde{u}^\dagger \tilde{v} + \frac{T_0 \rho_{0y}}{\rho_0 \gamma M^2} \tilde{\rho}^\dagger \tilde{v} + \frac{\rho_0 T_{0y}}{T_0 \gamma(\gamma-1)M^2} \tilde{T}^\dagger \tilde{v} \right] dy + \text{c.c.} \tag{46}$$

survives in the inviscid limit. It is clear that the energy transfer from the mean flow occurs via the Reynolds stress $(\tilde{u}^\dagger \tilde{v})$ and the coupling of the normal perturbation velocity with density $(\tilde{\rho}^\dagger \tilde{v})$ and temperature $(\tilde{T}^\dagger \tilde{v})$. The last two contributions $(\tilde{\rho}^\dagger \tilde{v}$ and $\tilde{T}^\dagger \tilde{v})$ are unique to compressible flows. Further, Eqs. (37), (40), and (41) also suggest that this inviscid growth is due to the transfer of energy from mean flow to $\tilde{u}$, $\tilde{\rho}$, and $\tilde{T}$ via the fluctuation in the normal velocity, $\tilde{v}$. The continuity is satisfied by a mere readjustment of $\tilde{w}$ which need not grow due to this algebraic growth. The growth of $\tilde{u}$ eventually would give rise to *streaks*.

Figure 19 shows the optimal patterns of the perturbation velocity field at $t=100$, obtained from our reduced inviscid model, Eq. (45). Figure 19(a) shows the counter-rotating

streamwise vortices in the $(y\text{-}z)$ plane, and Fig. 19(b) shows the contours of streamwise velocity fluctuation $\tilde{u}$ in the same plane which exhibits the well-known *streaks*. The structural features of these vortices and streaks are strikingly similar to those obtained from the solution of full viscous equations. Therefore, the compressible inviscid Ellingsen-Palm solution, along with the constraint of null pressure fluctuations, captures all essential features of the algebraic growth of the full viscous equations.

V. SUMMARY AND CONCLUSION

The compressible plane Couette flow is linearly unstable to acoustic disturbances for a range of supersonic Mach numbers. We found that the effects of viscosity stratification and nonuniform shear rate are to *stabilize* the unstable modes at large streamwise wave number (α) and Mach numbers (M). For a given Mach number, the critical Reynolds number (Re) is found to be significantly smaller (by a factor of 3 or more) in the uniform shear flow than in its nonuniform shear counterpart; for a given Re, the maximum growth rate (over all α, cf. Fig. 2) could be larger by an order of magnitude in the former. This strong stabilization effect appears to be tied to the strong viscosity stratification in nonuniform shear flow, and, therefore, *the viscosity stratification would lead to a delayed transition in compressible Couette flow*. Three-dimensional modes could be more unstable than their two-dimensional counterparts for some values of α, and hence Squire's theorem is, in general, not valid for the "nonisothermal" compressible Couette flow. It is shown that the mode II remains the *dominant* instability [i.e., the mode having the maximum growth rate over all α, Eq. (14)] for all Mach numbers in the uniform shear flow. In contrast, for the nonuniform shear flow, the mode I is the *dominant* instability for low Mach numbers and the mode II for moderate-to-large Mach numbers. For both mean flows, the viscosity plays the dual role of destabilizing (at small α) and stabilizing (at moderate-to-large α) the mode-II instability, but it destabilizes the mode-I instability. The higher-order odd (III,…) and even (IV,…) inviscid modes could also become unstable, but they remain subdominant with respect to mode-I and mode-II instabilities.

An analysis based on the perturbation kinetic energies transfered by different terms of the governing equation has been carried out to understand the origin of modal instabilities. The instability is primarily caused by an excess transfer of energy from mean flow to perturbations for a band of streamwise wave numbers. It is found that the energy-transfer rate from the mean flow occurs close to the moving and isothermal top wall for mode I, whereas it occurs in the bulk of the flow domain for mode II. For 2D modes, the thermal-diffusion process tends to stabilize the fluctuations at a higher rate than the viscous dissipation; for 3D modes, however, the viscous dissipation dominates over thermal diffusion at high spanwise wave number.

For the transient growth analysis, it is shown that the maximum temporal growth of perturbation energy, $G_{\max}$, and the corresponding time scale to attain this maximum, $t_{\max}$, are much larger (and can differ by a factor of 5 or more) for the uniform shear flow in comparison with the nonuniform shear flow. (In other words, the viscosity stratification has a strong stabilizing effect on transient energy growth.) Therefore, the uniform shear flow is more susceptible to *subcritical* transitions than its nonuniform shear counterpart. For both mean flows, the optimal energy growth G_{opt} [i.e., the global maximum of $G_{\max}$ in the (α,β) plane for given Re and M], decreases with increasing M; pure streamwise vortices $(\alpha_{\text{opt}}=0)$ are the optimal velocity patterns at large M, but the modulated streamwise vortices $(\alpha_{\text{opt}}\neq 0)$ are optimal patterns for low-to-moderate values of M. The physical mechanism of transient energy growth is tied to the transfer of energy from the mean flow to perturbations via the Reynolds stress and the coupling of density and temperature perturbations with the normal velocity.

For the streamwise independent perturbations $(\alpha=0)$, we have found that the transient energy growth follows the well-known scaling law, $G_{\max}\sim \mathrm{Re}^2$ and $t_{\max}\sim \mathrm{Re}$, of incompressible shear flow [3]. This is in stark contrast to the result on the nonuniform shear flow for which the above scaling law does not hold [18]. An analysis of the linear stability operator, $\mathcal{L}$, shows that $\mathcal{L}$ can be partitioned into a Re-dependent operator, $\mathcal{L}_p$, and a Re-independent operator, $\bar{\mathcal{L}}$ [Eqs. (27) and (31)] via the Mack transformation. The (in)validity of the above scaling laws for the (non)uniform shear flow is shown to be tied to the (non-)negligible contribution (to perturbation energy) of $\mathcal{L}_p$. Lastly, a "reduced" inviscid model [Eq. (45)], based on the inviscid Ellingsen-Palm-type solution, has been derived which captures all salient features of transient energy growth of full viscous equations.

APPENDIX: EVOLUTION EQUATION OF PERTURBATION ENERGY

It can be verified that the perturbation energy $\mathcal{E}(\alpha,\beta,t)$ satisfies the following time-evolution equation [18]:

$$\frac{\partial \mathcal{E}}{\partial t} = -i\int_0^1 \tilde{\mathbf{q}}^\dagger \mathcal{M}\mathcal{L}\tilde{\mathbf{q}}\,dy + \text{c.c.} = \dot{\mathcal{E}}_0 + \dot{\mathcal{E}}_1 + \dot{\mathcal{E}}_2 + \dot{\mathcal{E}}_3 + \dot{\mathcal{E}}_4. \tag{A1}$$

The constituent energy transfer rates $\dot{\mathcal{E}}_0$–$\dot{\mathcal{E}}_4$ have the following forms (with $D=d/dy$):

$$\dot{\mathcal{E}}_0 = -i\alpha\int_0^1 U_0 \tilde{\mathbf{q}}^\dagger \mathcal{M}\tilde{\mathbf{q}}\,dy + \text{c.c.}, \tag{A2}$$

$$\dot{\mathcal{E}}_1 = -\int_0^1 \left[\rho_0 U_{0y}\tilde{u}^\dagger\tilde{v} + \frac{T_0\rho_{0y}}{\rho_0\gamma M^2}\tilde{\rho}^\dagger\tilde{v} + \frac{\rho_0 T_{0y}}{T_0\gamma(\gamma-1)M^2}\tilde{T}^\dagger\tilde{v}\right]dy + \text{c.c.}, \tag{A3}$$

$$\dot{\mathcal{E}}_2 = -\frac{1}{\mathrm{Re}}\int_0^1 [\alpha^2(\mu_0+\lambda_0)\tilde{u}^\dagger\tilde{u} + \mu_0(\alpha^2+\beta^2)\tilde{u}^\dagger\tilde{u} - \tilde{u}^\dagger(\mu_{0y}D + \mu_0 D^2)\tilde{u} - i\alpha\tilde{u}^\dagger[\mu_{0y} + (\mu_0+\lambda_0)D]\tilde{v} + \alpha\beta(\mu_0+\lambda_0)\tilde{u}^\dagger\tilde{w} - (U_{0yy}\mu_T + U_{0y}T_{0y}\mu_{TT})\tilde{u}^\dagger\tilde{T} - U_{0y}\mu_T\tilde{u}^\dagger D\tilde{T} - i\alpha\tilde{v}^\dagger[\lambda_{0y} + (\mu_0+\lambda_0)D]\tilde{u} + \mu_0(\alpha^2+\beta^2)\tilde{v}^\dagger\tilde{v} - \tilde{v}^\dagger[(\lambda_{0y}+\mu_{0y})D + (\lambda_0+\mu_0)D^2 + \mu_{0y}D + \mu_0 D^2]\tilde{v} - i\beta(\lambda_0+\mu_0)\tilde{v}^\dagger D\tilde{w} - i\alpha U_{0y}\mu_T\tilde{v}^\dagger\tilde{T} - i\beta\lambda_{0y}\tilde{v}^\dagger\tilde{w} - i\beta\mu_{0y}\tilde{w}^\dagger\tilde{v} + \alpha\beta(\mu_0+\lambda_0)\tilde{w}^\dagger\tilde{u} - i\beta(\lambda_0+\mu_0)\tilde{w}^\dagger D\tilde{v} + [\mu_0(\alpha^2+\beta^2) + \beta^2(\lambda_0+\mu_0)]\tilde{w}^\dagger\tilde{w} - \mu_0\tilde{w}^\dagger D^2\tilde{w} - \mu_{0y}\tilde{w}^\dagger D\tilde{w}]dy + \text{c.c.}, \tag{A4}$$

$$\dot{\mathcal{E}}_3 = \frac{1}{\sigma\,\mathrm{Re}(\gamma-1)M^2}\int_0^1 \rho_0\tilde{T}^\dagger[\mu_T T_{0yy} + T_{0y}^2\mu_{TT} + 2T_{0y}\mu_T D - (\alpha^2+\beta^2)\mu_0 + \mu_0 D^2]\tilde{T}dy + \text{c.c.}, \tag{A5}$$

$$\dot{\mathcal{E}}_4 = \frac{1}{\mathrm{Re}}\int_0^1 \rho_0[2\mu_0 U_{0y}\tilde{T}^\dagger D\tilde{u} + 2i\alpha\mu_0 U_{oy}\tilde{T}^\dagger\tilde{v} + U_{0y}^2\mu_T\tilde{T}^\dagger\tilde{T}]dy + \text{c.c.} \tag{A6}$$

Here, $\dot{\mathcal{E}}_1$ is the energy transfer rate from the mean flow, $\dot{\mathcal{E}}_2$ the viscous dissipation rate, $\dot{\mathcal{E}}_3$ the thermal diffusion rate and $\dot{\mathcal{E}}_4$ the shear-work rate, respectively; note that the convective transfer of perturbation energy by the mean flow, $\dot{\mathcal{E}}_0$, is zero.

[1] P. G. Drazin and W. H. Reid, *Hydrodynamic Stability* (Cambridge University Press, Cambridge, 1985).
[2] W. M. F. Orr, Proc. R. Ir. Acad., Sect. A **27**, 9 (1907).
[3] L. H. Gustavsson, J. Fluid Mech. **224**, 241 (1991).
[4] K. M. Butler and B. F. Farrell, Phys. Fluids A **4**, 1637 (1992).
[5] L. N. Trefethen, A. E. Trefethen, S. C. Reddy, and T. A. Driscoll, Science **261**, 578 (1993).
[6] S. C. Reddy, P. J. Schmid, and D. S. Henningson, SIAM J. Appl. Math. **53**, 15 (1993).
[7] T. Gebhardt and S. Grossmann, Phys. Rev. E **50**, 3705 (1994).
[8] A. Hanifi, P. J. Schmid, and D. S. Henningson, Phys. Fluids **8**, 826 (1996).
[9] A. Schmiegel and B. Eckhardt, Phys. Rev. Lett. **79**, 5250 (1997).
[10] B. F. Farrell and P. J. Ioannou, Phys. Fluids **12**, 3021 (2000).
[11] J. Kim and J. Lim, Phys. Fluids **12**, 1885 (2000).
[12] D. S. Pradeep and F. Hussain, J. Fluid Mech. **550**, 251 (2006).
[13] P. J. Schmid, Annu. Rev. Fluid Mech. **39**, 129 (2007).
[14] B. Eckhardt, T. M. Schneider, B. Hof, and J. Westerwell, Annu. Rev. Fluid Mech. **39**, 447 (2007).
[15] S. Grossmann, Rev. Mod. Phys. **72**, 603 (2000).
[16] A. Bottaro, P. Corbett, and P. Luchini, J. Fluid Mech., **476**, 293 (2003).
[17] C. Nouar, A. Bottaro, and J. P. Brancher, J. Fluid Mech. **592**, 177 (2007).
[18] M. Malik, M. Alam, and J. Dey, Phys. Fluids **18**, 034103 (2006).
[19] P. W. Duck, G. Erlebacher, and M. Y. Hussaini, J. Fluid Mech. **258**, 131 (1994).
[20] S. Hu and X. Zhong, Phys. Fluids **10**, 709 (1998).
[21] W. Glatzel, J. Fluid Mech. **202**, 515 (1989).
[22] L. M. Mack, AGARD Rep. **709**, 3-1 (1984).
[23] M. R. Malik, J. Comput. Phys. **86**, 76 (1990).
[24] M. Malik, M. Alam, and J. Dey (unpublished).
[25] T. Ellingsen and E. Palm, Phys. Fluids **18**, 487 (1975).
[26] A. Hanifi and D. S. Henningson, Phys. Fluids **10**, 1784 (1998).